

RSC Advances



This is an *Accepted Manuscript*, which has been through the Royal Society of Chemistry peer review process and has been accepted for publication.

Accepted Manuscripts are published online shortly after acceptance, before technical editing, formatting and proof reading. Using this free service, authors can make their results available to the community, in citable form, before we publish the edited article. This *Accepted Manuscript* will be replaced by the edited, formatted and paginated article as soon as this is available.

You can find more information about *Accepted Manuscripts* in the [Information for Authors](#).

Please note that technical editing may introduce minor changes to the text and/or graphics, which may alter content. The journal's standard [Terms & Conditions](#) and the [Ethical guidelines](#) still apply. In no event shall the Royal Society of Chemistry be held responsible for any errors or omissions in this *Accepted Manuscript* or any consequences arising from the use of any information it contains.

Cite this: DOI: 10.1039/c0xx00000x

www.rsc.org/xxxxxx

ARTICLE TYPE

Exploration of the electrochemical mechanism of ultrasmall multiple phases molybdenum carbides nanocrystals for hydrogen evolution reaction

*Chunyang He^{*a,b}, Juzhou Tao^{*a,b}**Received (in XXX, XXX) Xth XXXXXXXXXX 20XX, Accepted Xth XXXXXXXXXX 20XX*

DOI: 10.1039/b000000x

Sustainable and affordable hydrogen production through splitting of water, an essential step towards renewable and clean energy storage, calls for efficient non-precious-metal catalyst to make the process economically viable. Ultrasmall multiple phases molybdenum carbides nanocrystals (2.5 nm for MoC and 5.0 nm for Mo₂C) on graphene support were synthesized by a simple in situ method. Both molybdenum carbide on graphene hybrid materials, the MoC-G and the Mo₂C-G, show extraordinary high activity for hydrogen evolution reaction (HER) in acid media. The reaction kinetics of the MoC-G and Mo₂C-G were revealed. The X-ray photoelectron spectroscopy (XPS) and X-ray absorption fine structure (XAFS) were conducted to study the electronic nature of MoC-G and Mo₂C-G electrocatalysts to explore the electrochemical mechanism of ultrasmall multiple phases molybdenum carbides nanocrystals for hydrogen evolution reaction.

Introduction

Hydrogen, a clean energy carrier with the highest energy content for any chemical energy storage, can produce electricity efficiently through reversible hydrogen fuel cell.^{1,2} A vision of the hydrogen economy coupling such renewable energy sources as solar, wind, tidal and geothermal energy to the hydrogen energy carrier holds the potential of solving the twin problems of global climate change and fossil fuel exhaustion in one stroke.³ Indispensable to this technology paradigm is economical and sustainable hydrogen production through water splitting, which requires efficient and affordable electrocatalysts to promote the hydrogen evolution reaction (HER) but remains an open technical challenge.⁴ Among a wide variety of available catalysts, Pt-based are the most efficient ones for HER, capable of driving significant current at extremely low overpotential with small Tafel slope.⁵⁻⁷ Hence efficient and affordable HER catalysts with high electrochemical durability are needed to replace the costly and extremely low-abundance-Pt-based catalysts to realize sustainable hydrogen production.⁸⁻¹¹ Amid considerable recent efforts in this direction, some successful examples are transitional metal chalcogenides (MoS₂,¹²⁻¹⁴ WS₂,⁴ FeS₂¹⁵), phosphides (Ni₂P,^{16, 17} CoP,^{18, 19} MoP,²⁰ FeP²¹), nitride (Co_{0.6}Mo_{1.4}N₂,²² NiMoN_x/C²³) and metal-free carbon nitride based materials.^{24, 25}

Due to the unique d-band electronic structure and similarity of

their electronic states to noble Pt at the Fermi level, group VI transition metal carbides exhibit catalytic properties analogous to Pt.²⁶⁻²⁸ One such carbide, Molybdenum carbide, has been widely employed as a catalyst for methanol steam reforming,²⁹ methane reforming,³⁰ water gas shift reaction,³¹ oil conversion,³² etc. It has also received attention as a support material for noble metals to enhance oxygen reduction and methanol oxidation activity.^{33, 34} Recently, Xu et al. investigated electrochemical activity and stability of commercial molybdenum carbides towards HER in both acidic and basic solutions.³⁵ Since catalytic properties of molybdenum carbides depend strongly on their surface configurations, microstructure and electronic states,³⁶ at least five approaches exist to optimize its HER activity: (i) increasing surface density of active sites to accelerate the interfacial electrocatalytic reactions;³⁶ (ii) constructing high surface area scaffold electrode to facilitate circulation of ions and H₂;³⁷ (iii) supporting with a suitable carrier to form highly dispersed system, increasing durability and promoting electron transfer when coupled with a high conductivity carrier;^{36, 38} (iv) building specific nanostructures;^{39, 40} (v) substituting with such transition metals as Co or Ni to form bimetallic sites and modify the catalytic properties.⁴¹ Decreasing molybdenum carbide grain size is the most direct and efficient approach to increase the number of electronically connected active sites per unit geometric area, which is closely associated with catalytic activity. Chen et al.

Cite this: DOI: 10.1039/c0xx00000x

www.rsc.org/xxxxxx

ARTICLE TYPE

presented an biomass-derived molybdenum carbide of 9.4 nm in size, one of the smallest particle size molybdenum carbide as HER catalyst.⁴² Yan et al. successfully synthesized molybdenum carbide nanoparticles down to 2 nm in size on carbon through an ion exchange process, which served as an efficient non-noble metal catalyst support for fuel cell application.⁴³ However carbonization of the organics in the catalyst preparation resulted in carbon coating layer on the catalyst surface, which may block the active sites of the molybdenum carbide. In the present paper, we report preparation of ultra-small molybdenum carbides nanocrystals, 2.5 nm for MoC and 5.0 nm for Mo₂C, on graphene support through a simple *in situ* synthesis method. The as-synthesized products show a highly dispersed distribution of clean surface nanoparticles on the graphene support, which provides a large surface area and high conductivity to facilitate the HER through enhanced mass and electron transfer. The fast reaction kinetics of the MoC-G and Mo₂C-G were revealed. The electrochemical mechanism of ultrasmall multiple phases (cubic MoC and β-Mo₂C) molybdenum carbides nanocrystals for hydrogen evolution reaction were explored by XPS and XAFS, unraveling the charge-transfer from molybdenum to carbon and synergetic chemical coupling effects between the molybdenum carbide nanocrystals and the graphene support.

Experimental

Synthesis of MoC-G and Mo₂C-G

The details of MoC-G and Mo₂C-G preparation and electrochemical activity characterisations were reported in our previous paper⁴⁴. The typical procedure for preparing molybdenum carbides on graphene sheets (MoC-G and Mo₂C-G) is shown in Scheme 1, which are described in the following sections. 0.8 g graphene oxide (GO) was first dissolved in 200 mL deionized water in a beaker sonicated for 2 h. 0.36g (NH₄)₆Mo₇O₂₄ · 4H₂O was dissolved in 50 mL deionized water in a beaker, then the resulted solution poured into the GO suspension sonicated for 30 min. The mixture was dried at 90 °C until turning into hydrogel-like mixture then freeze dried. Further annealing in a tube furnace under Argon at 750 °C and 900 °C for 2 h forms molybdenum carbides. Ramping rate in tube furnace was controlled at 5 °C min⁻¹ and the final products were cooled down to 30 °C in the tube furnace at 10 °C min⁻¹. The annealing temperature is 750 °C for MoC-G and 900 °C for Mo₂C-G.

More experimental details are seen in the Supporting Information.

Characterizations

X-ray diffraction (XRD) was performed on a Rigaku D/Max-III using Cu K α radiation operating at 30 kV and 30 mA. 2 θ angular regions between 10° and 80° were measured at a scan rate of 6° min⁻¹. X-ray photoelectron spectroscopy (XPS) measurements were carried out on an XPS apparatus (ESCALAB 250, Thermo-VG Scientific Ltd.). Transmission electron microscopy

(TEM) were performed on a field emission transmission electron microscope (FETEM, FEI Tecnai G2 F30) operating at 300 kV. N₂ adsorption experiments using an ASAP 2020 Surface Area Analyzer (Micromeritics Co., USA) were conducted to investigate sample porosity. Mo *K*-edge X-ray absorption spectroscopy (XAS) of a Mo foil standard and catalyst samples were recorded in total electron yield transmission mode at the beamline BL14W1 of the Shanghai Synchrotron Radiation Facility (SSRF), China.

The HER experiments were conducted on an Autolab PGSTAT 302 (ECO Chemie, Netherlands) at 25 °C in a thermostatic water bath. Linear sweep voltammetry (LSV) tests were performed in 0.5 M H₂SO₄ at 5 mV s⁻¹ scan rate. Electrochemical impedance spectroscopy (EIS) measurements were recorded at frequency range of 100 kHz to 100 MHz with modulation amplitude of 10 mV.

For comparison, 46.7wt% platinum on VC-72 catalyst (Pt/C from TKK, Japan) was measured under identical conditions, the loading is 12.5 $\mu\text{g cm}^{-2}$ for Pt metal.

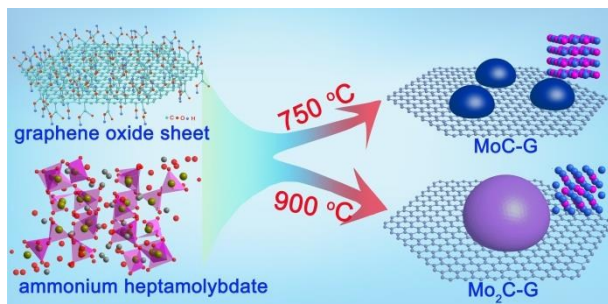
Results and Discussions

Figure S1a displays X-ray diffraction (XRD) pattern of the MoC-G indexed as a typical cubic structure (Fm-3m(225)), indicated by the magenta vertical lines (PDF#65-0280). Mo₂C with Fe₂N structure (hexagonal, P63/mmc(194)) was also formed on graphene as Mo₂C-G, indicated by the red vertical lines (PDF#35-0787) shown in Figure S1b. Figure S2a and Figure S2b shows the typical bright field TEM image of the MoC-G and Mo₂C-G, respectively. The MoC and Mo₂C nanoparticles (NPs) are homogeneously dispersed on the graphene sheet surface, no agglomeration is observed. In the HRTEM images (Figure S2b-c and Figure S2e-f), lattice fringes of the MoC and Mo₂C nanocrystals were clearly observed, indicating excellent crystallization of the latter. The MoC and Mo₂C nanocrystals are ultra-small, their mean particle size, calculated from more than 200 nanocrystals, are 2.5 nm and 5.0 nm, respectively, according to particle size distribution (Figure S3). The detailed microstructures of the MoC and Mo₂C were further characterized by high-angle annular dark-field scanning transmission electron microscopy (HAADF-STEM) analysis. Typical HAADF-STEM images of the MoC-G and Mo₂C-G are shown in Figure 1 and 2c, respectively. Figure 1b and 1d show their corresponding atomic-resolution HAADF-STEM images. Clearly no surface contamination or surface coating exist on the surface of the MoC and Mo₂C nanocrystals, presenting an extremely clean surface which is absolutely crucial to the HER. In contrast to most of the reported synthesis methods of nanostructured molybdenum carbide down to 10 nm that require addition of such organic compounds as urea,³⁸ soybeans⁴² and ion exchange resin⁴³, which results in surface contamination or surface coating and blocking of the active sites, our synthesis is achieved through local exchange of active carboxyl and hydroxyl groups on the

Cite this: DOI: 10.1039/c0xx00000x

www.rsc.org/xxxxxx

graphite oxide with $\text{Mo}_7\text{O}_{24}^{6-}$ ions at the ionic level, producing MoC and Mo_2C NPs with definitely clean surface.



Scheme 1 Schematic diagram of the MoC-G and Mo₂C-G synthesis.

The porosity of MoC-G and Mo₂C-G composites was determined by the nitrogen adsorption/desorption isothermal measurements at 77 K. As shown in Figure S4a, the Brunauer-Emmett-Teller (BET) surface area of MoC-G and Mo₂C-G composites are 344 and 278 m² g⁻¹, respectively. The pore size distribution and total pore volume of the composite were calculated based on the DFT model. Figure S4b shows the cumulative pore volumes of MoC-G and Mo₂C-G nanocomposites. The corresponding density functional theory (DFT) pore size distribution (Figure S4c) exhibits a hierarchical pore structure that include micro- (< 2 nm), meso- (2-50 nm), and macropores (> 50 nm). The large surface area can substantially increase the number of active sites by increasing contact area between catalysts and electrolyte, and the well-developed porosity structures could facilitate transfer of reactants and products, which enhances mass transport and thus increases the HER efficiency.⁴⁵

Figure 2a compares the measured electrocatalytic activity of polarization curves (*i*-*V* plot) using linear sweep voltammetry (LSV). On all three electrodes, applying electrochemical potential below 0 V initializes the reduction process. Hydrogen bubbles evolved more vigorously on the electrodes at higher overpotential, except the graphene barely shows electrocatalytic activity towards the HER. Among the three catalysts, the Pt/C catalyst exhibited the lowest overpotential (η_{10} =35 mV) at 10 mA cm⁻² of cathodic current density. Figure 2b zooms in on the dotted region in 2a, with the Mo₂C-G possessing nearly zero onset overpotential very close to the Pt/C. The HER activity of Mo₂C-G is exceptional with small overpotentials of 150 mV (η_{10}) and 170 mV (η_{20}) at 10 and 20 mA cm⁻² cathodic current density respectively. Figure 2b also shows that the onset overpotential of the MoC-G shifts 15 mV down to negative potential compared with Mo₂C-G. The overpotential (η_{10}) of MoC-G at 10 mA cm⁻² cathodic current density is 221 mV.

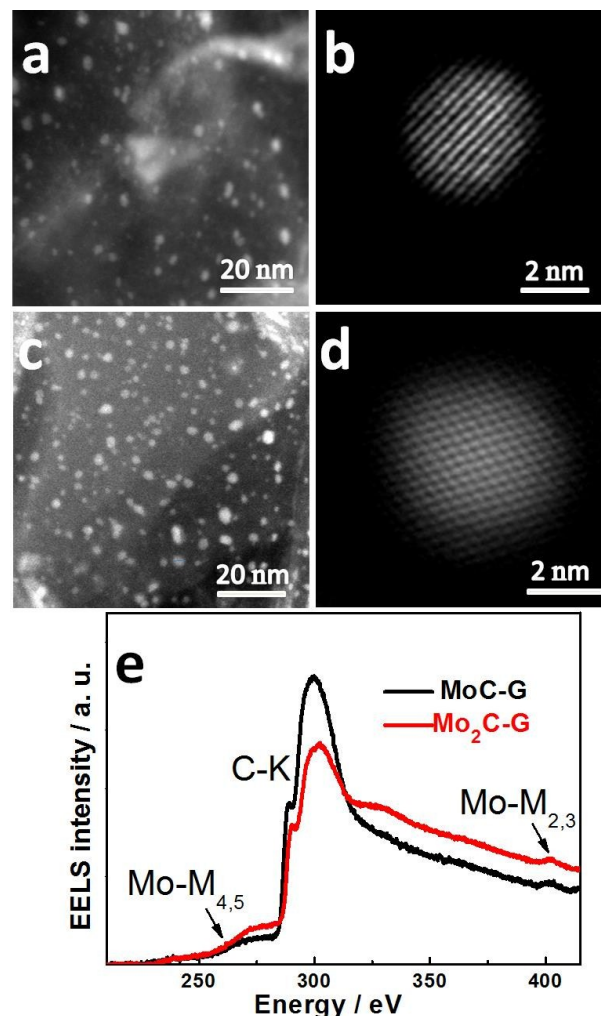


Fig. 1 (a) HAADF-STEM image of MoC-G nanocomposite, (b) atomic-resolution HAADF-STEM image of an individual MoC nanocrystal, (c) HAADF-STEM image of Mo₂C-G nanocomposite, (d) atomic-resolution HAADF-STEM image of an individual Mo₂C nanocrystal, (e) EELS profile of the as-synthesized MoC-G and Mo₂C-G nanocomposites.

Electrochemical impedance spectroscopy (EIS) at different HER overpotentials was further conducted to investigate underlying electrochemical mechanism of the HER process for the synthesized catalysts. The Bode plots recorded at η =100 mV as shown in Figure 2c suggest a classical one-time-constant process for bulk Mo₂C and the presence of a two-time-constant process for MoC-G and Mo₂C-G. The first one at higher frequency is attributed to the large surface area and well-developed porosity structures of MoC-G and Mo₂C-G, which confirmed by the BET results, the other one at lower frequency is related to the HER process⁴⁶⁻⁴⁸. Representative Nyquist plots collected at η =100 mV on the bulk Mo₂C, MoC-G and Mo₂C-G electrodes are compared in Figure 2d. A

Cite this: DOI: 10.1039/c0xx00000x

www.rsc.org/xxxxxx

ARTICLE TYPE

two-time-constant model was applied to describe the response of the HER process on MoC-G and Mo₂C-G^{36, 49}, as shown in Figure S5. In this model, R_c represents the contact resistance of between the glassy carbon electrode and the catalyst layer and R_{sol} represents the solution resistance, connects in series with two additional branches: one is related to the charge-transfer process (CPE1- R_{ct}); the other to the surface porosity (CPE2- R_p). The charge-transfer resistance R_{ct} , determined from the semicircle registered at low frequencies, reflects the HER kinetics, a smaller R_{ct} value corresponding to faster kinetics. R_{ct} of Mo₂C-G is 10.4 Ω at $\eta=100$ mV, lower than 35.9 Ω for MoC-G and much lower than 2757 Ω for bulk Mo₂C, suggesting faster reaction kinetics for Mo₂C-G. Since R_{ct} decrease with increasing applied potential, even faster HER kinetics will occur at higher overpotential.

various catalysts. The Tafel plots from voltammetry data were fitted to the Tafel equation ($\eta = a+b*\log|j|$), where j is the current density and b the Tafel slope, as shown in Figure S6b. The Tafel slope of Pt/C is 30 mV dec⁻¹. The HER on a Pt surface is known to proceed through the Volmer–Tafel reaction mechanism, with fast discharge reaction and H₂ evolving by a rate-determining combination reaction, i.e., the Tafel step⁵⁰. The Tafel slope of bulk Mo₂C is 116 mV dec⁻¹ (Figure S6b), which suggests the discharge reaction is slow and the Volmer step is the rate-determining step. The Tafel slope of 57 mV dec⁻¹ was observed for Mo₂C-G (Figure S6b), which is much smaller than that of bulk Mo₂C and suggests faster proton discharge kinetics and more efficient hydrogen evolution. The Tafel slope of MoC-G is 88 mV dec⁻¹, smaller than what has been previously reported for γ -MoC (hexagonal structure, P-6m2, 121.6 mV dec⁻¹)⁵¹. For the Tafel slope values of 57 mV dec⁻¹ and 88 mV dec⁻¹ (Figure S6b), one possible pathway for HER is through a Volmer–Heyrovsky reaction mechanism, and the rate determining step could be discharge reaction or electrochemical desorption of H_{ads} and H₃O⁺ to form hydrogen. However, Tafel slope obtained from voltammetry data usually includes contributions from electron transport resistance (RET) of catalysts, which is highly dependent on the scalability of catalyst use (i.e. increased RET in thicker catalyst films)³⁹. Vrabel et al. developed a method based on electrochemical impedance spectroscopy to circumvent this issue⁵². Using this method, the plot of $\log R_{ct}^{-1}$ vs. overpotential also gives the Tafel slope, which reflects purely the charge transfer kinetics. The Nyquist plot for Mo₂C-G between 0 and 200 mV overpotential is presented in Figure 2e, the same plots for bulk Mo₂C and MoC-G are shown in Figure S7. From the Figure 2e and Figure S7, we can obtain the R_{ct} of Mo₂C-G, bulk Mo₂C and MoC-G at different overpotentials (Table S2), and further acquire the plot of $\log R_{ct}^{-1}$ vs. overpotential (Figure 2f). The Tafel slope of bulk Mo₂C is 88 mV dec⁻¹ from the EIS data, in accordance with the previous reported values also from the EIS data^{36, 42}. This value is however much smaller than 116 mV dec⁻¹ obtained from the voltammetry data, suggesting the RET is significant for the bulk Mo₂C. The Tafel slopes of MoC-G and Mo₂C-G from the EIS data are 80 mV dec⁻¹ and 55 mV dec⁻¹, respectively, which are only slightly smaller than those from the voltammetry data (88 mV dec⁻¹ and 57 mV dec⁻¹), suggesting low RET or high electrical conductivity of MoC-G and Mo₂C-G. The Tafel slope of Mo₂C-G (55 mV dec⁻¹) from the EIS data is still significantly lower than that of bulk Mo₂C (88 mV dec⁻¹), indicating an intrinsic faster charge transfer kinetics, which likely derives from the interaction between the graphene sheet and Mo₂C NPs.

High durability is an indispensable characteristic for the catalyst in practical application, but it is still a great challenge to prepare the catalyst in line with the requirements of the high durability of the catalyst for HER in acid electrolyte. The cyclic voltammograms of MoC-G and Mo₂C-G electrodes obtained before and after 2,000 cycles are shown in Figure S8a-b. No

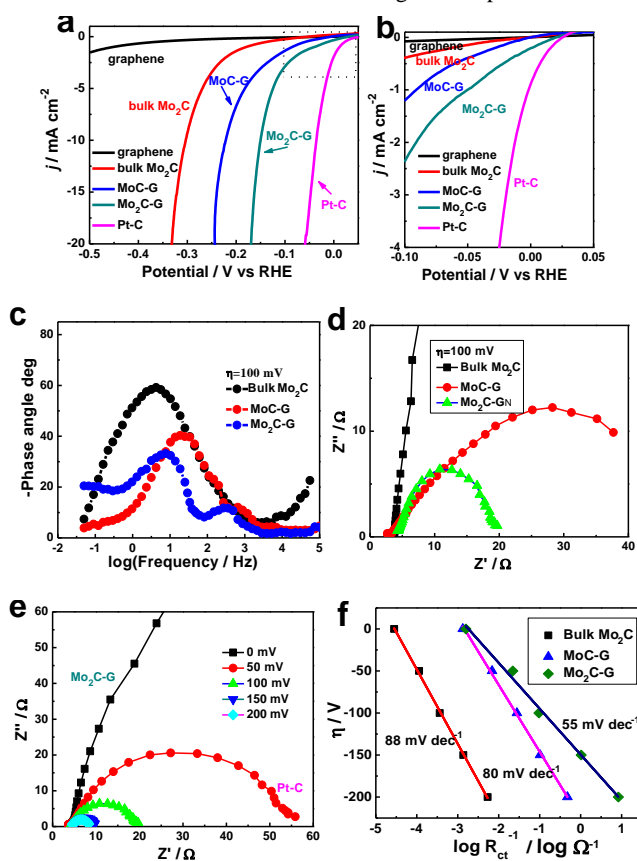


Fig. 2 (a) Polarization curves of bulk Mo₂C, MoC-G, Mo₂C-G, Pt/C and graphene, (b) zoom-in of the dotted region in (a). Bode (c) and Nyquist (d) plots showing EIS responses of bulk Mo₂C, MoC-G, Mo₂C-G electrodes at HER overpotential of 100 mV in 0.5 mol L⁻¹ H₂SO₄, (e) Nyquist plots showing EIS responses of Mo₂C-G electrode at various HER overpotentials, (f) semi-logarithmic plot of the inverse charge-transfer resistance ($\log R_{ct}^{-1}$), as a function of overpotential (η).

Tafel analysis was also applied to both the voltammetry data and EIS data to probe the predominant HER mechanism of the

Cite this: DOI: 10.1039/c0xx00000x

www.rsc.org/xxxxxx

ARTICLE TYPE

obvious degradation occur on both MoC-G and Mo₂C-G electrodes. The high durability of MoC-G and Mo₂C-G also examined by the long-term stability test (Figure S8c). After a long period of 20 h, the current density on the MoC-G and Mo₂C-G electrodes only show negligible degradation, which could be due to the consumption of proton in the system and the hindrance of the reaction by hydrogen bubbles remaining on the electrodes.

To investigate the microstructure of MoC-G and the Mo₂C-G after electrocatalytic activity testing, the catalysts were collected by sonicating the glassy carbon disk electrode in ethanol after the electrocatalytic durability testing, and observed by TEM. Figure S9 display the TEM and HRTEM images of MoC-G and

Mo₂C-G after electrocatalytic durability testing, revealing no obvious particle coalescence and aggregation. The HRTEM images of MoC-G after electrocatalytic durability testing shows the lattice fringes which measured 0.247 nm, consistent with the (111) crystal plane of MoC. The HRTEM images of Mo₂C-G after electrocatalytic durability testing clearly resolved interplanar distances are measured 0.260 nm and 0.227 nm, corresponding to the (10 $\bar{1}$ 0) and (10 $\bar{1}$ 1) crystal planes of the Mo₂C. These results indicate that both of the morphology and microstructure of MoC-G and Mo₂C-G have no obvious change after electrocatalytic durability testing, which is the origin of the highly electrocatalytic durability of MoC-G and Mo₂C-G.

Table 1 The HER performances of the various catalysts.

Catalyst	E ₀ ^a / mV	η ₁₀ ^b / mV	η ₁₀ ^b / mV	Tafel slope / mV dec ⁻¹		j ₀ ^e / mA cm ⁻²	R _{ct} ^f / Ω
				c	d		
Bulk Mo ₂ C	117	304	/	116	88	3.80×10 ⁻³	2757
MoC-G	30	221	229	88	80	2.55×10 ⁻²	35.9
Mo ₂ C-G	~0	150	156	57	55	2.58×10 ⁻²	10.4
Pt/C	~0	36	/	30	/	2.79×10 ⁻¹	/

^a onset potential of the various catalysts. ^b Overpotential at 10 mA cm⁻² after potential sweeps for 2,000 cycles between -0.3 and +0.2 V vs. RHE. ^c From Tafel equation. ^d From logR_{ct}⁻¹ vs. η. ^e exchange current density calculated from Tafel plots. ^f Charge-transfer resistance that extracted from fitting electrochemical impedance spectra measured at η = 100 mV to an equivalent circuit.

The composition and surface electronic states of MoC-G and Mo₂C-G were investigated by X-ray photoelectron spectroscopy (XPS). Bulk Mo₂C and MoO₃-G were also examined for comparison. The survey XPS spectrum (Figure S10) indicates that all of the samples are composed of C, Mo, and O elements. As shown in Figure 3, all of the deconvoluted profiles of MoO₃-G, bulk Mo₂C, MoC-G and Mo₂C-G contain MoO₃ and MoO₂, suggesting that MoC and Mo₂C are prone to oxidation on the graphene surface, in agreement with the previous studies^{41,53}. The MoO₃ in Figure 3a possesses doublet peaks of 236.0 and 232.8 eV for Mo 3d_{3/2} and Mo 3d_{5/2} with a spin energy separation of ~3.2 eV, the two peaks were assigned to Mo⁴⁺ and Mo⁶⁺. The detection of molybdenum oxides is attributed to surface oxides formation when exposed to air⁵³. Figure 3b displays the XPS Mo 3d spectra of bulk Mo₂C with three molybdenum species. A third peak with Mo 3d_{5/2} binding energy of 228.7 eV besides the doublet peaks is present and attributed to Mo²⁺ species involved in Mo-C bonding³⁰. Figure 3c and 3d displays the XPS Mo 3d spectra of MoC-G and Mo₂C-G, respectively. In addition to the molybdenum oxides identified as Mo⁴⁺ and Mo⁶⁺ that are clearly present, a portion of Mo species is in the form of carbides in both MoC-G and Mo₂C-G.

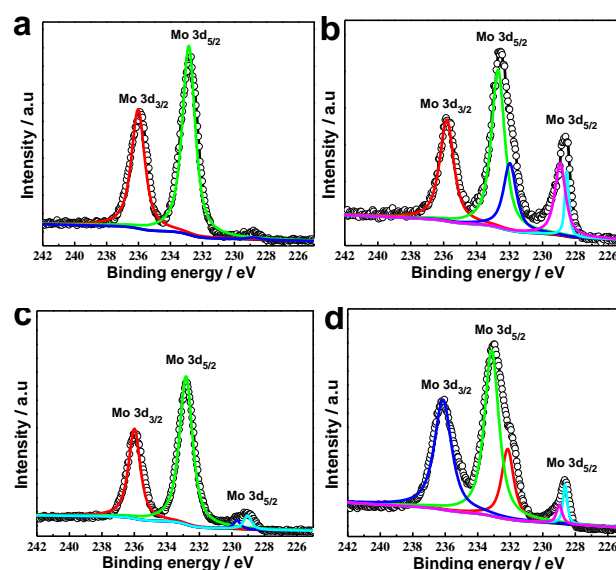


Fig. 3 XPS Mo 3d spectra (without background, black) and the fitted peaks of MoO₃-G (a), bulk Mo₂C (b), MoC-G (c) and Mo₂C-G (d).

Cite this: DOI: 10.1039/c0xx00000x

www.rsc.org/xxxxxx

ARTICLE TYPE

We further determined the charge states and electronic nature of the MoC-G and Mo₂C-G catalyst by X-ray absorption near-edge structure (XANES) and extended X-ray absorption fine structure (EXAFS) spectroscopies. Figure 4a shows the normalized XANES spectra at the Mo *K*-edge of the precursor (ammonium molybdate), Mo₂C-G and MoC-G, as well as MoO₃ and Mo foil standards. The absorption edge varies depending on the molybdenum oxidation state. The Mo *K*-edge XANES spectrum of the ammonium molybdate precursor shows similar pre-edge to that of MoO₃, which is ascribed to the Mo(VI) oxidation state. The absorption edges of Mo₂C-G and MoC-G catalysts, corresponding to an electric dipole transition from Mo 1s core level to unoccupied states of p type, were shifted to higher energies compared to the Mo foil. Correlation of the Mo *K* edge half step energy to the Mo valence state is examined in Figure 4b. The Mo foil refers to zero-valence state. The half-step energies of both Mo₂C-G and MoC-G catalysts were higher by ca. 2-4 eV compared to Mo foil, which may be caused by a negative charge-transfer from molybdenum to carbon^{36, 54}. Liu *et al.* have shown that the more positively charged the Mo atoms, the lower their d-band center⁵⁵. The down-shifted d-band center of Mo atoms increases the degree of d-band filling, thereby enhances the d-band charge density near the Fermi level and results in electronic localization of the Mo atoms making orbital overlapping with the H_{ads} in the HER process more difficult, which consequently decreases hydrogen binding energy, lowers activation energy of evolution H₂ from H_{ads} and gives rise to enhanced hydrogen evolution reaction. Youn *et al.* have noted that more positive charge implies higher HER activity³⁸.

Figure 4c and 4d display the Fourier transforms (FT) of *k*³-weighted Mo *K*-edge EXAFS spectra of Mo₂C-G and MoC-G, respectively. The differences between the Mo₂C-G and MoC-G are apparent, indicating significantly different atomic structures surrounding Mo in two catalysts. The Mo₂C-G spectrum was well fitted with the orthorhombic β-Mo₂C structure model, no oxide-related peaks are observed in the EXAFS. Whereas the MoC-G exhibits three distinct peaks, one of which at approximately 1.2 Å is assigned to Mo–O bond in oxide form. It has been found that oxide species form on the surface of molybdenum carbide nanoparticles³⁰, which is also confirmed by the above XPS data analysis. Thus, the higher half-step energies of MoC-G in Figure 4b partially derives from the formation of surface oxide species. This explains why the MoC-G possesses higher half-step energies but shows lower HER activity than the Mo₂C-G. The other two peaks in the MoC-G EXAFS spectrum are well fitted with a cubic MoC structure model. Table S3 summarizes the fitted parameters of the Mo₂C-G and MoC-G catalysts. We note that the lengths of Mo–Mo bond obtained for the Mo₂C-G (2.98 Å) and MoC-G (3.04 Å) are longer than that of pure Mo (2.73 Å).

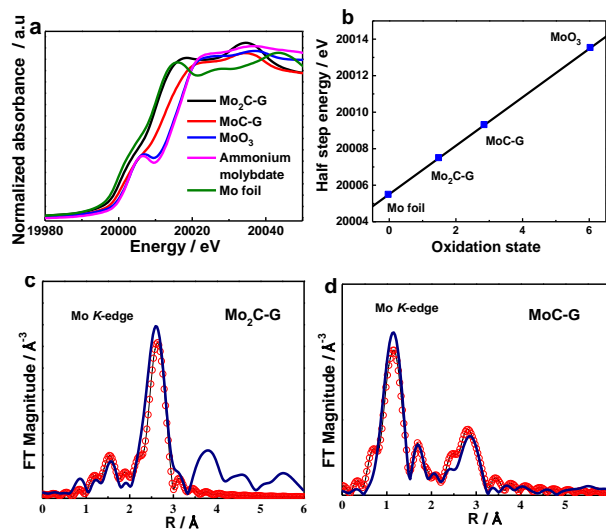


Fig. 4 (a) XANES spectra at the Mo *K*-edge from the Mo₂C-G, MoC-G, ammonium molybdate, MoO₃ and Mo foil, (b) correlation of the Mo *K*-edge half step energy to the oxidation state of various molybdenum species, *k*³-weighted Mo *K*-edge EXAFS Fourier transform magnitudes and first-shell fit of the Mo *K*-edge obtained from Mo₂C-G (c) and MoC-G (d).

Nanoparticles formed *in situ* are inlaid or anchored into graphene support and will lead to close bonding and synergetic coupling between the graphene and nanoparticles^{56, 57}. Chen *et al.* has also reported that molybdenum carbide catalysts thus formed develop covalent binding between nanoparticles and the carbon/CNTs support which provides unique coupling effects on electrochemical properties³⁶. The covalent binding interactions between graphene and molybdenum carbide nanoparticles, including charge-transfer and downshift of the d-band center of molybdenum, are likely the intrinsic origins of the enhanced HER performance of MoC-G and Mo₂C-G. In addition, the small size, clean surface, large surface area and hierarchical porous structure also facilitate the HER process on the MoC-G and Mo₂C-G.

Conclusions

In summary, we present a synthetic route to prepare different phases of ultra-small molybdenum carbide nanocrystals on graphene (MoC-G and Mo₂C-G). The Mo₂C-G catalyst exhibits an excellent HER activity of one of the smallest overpotential close to 0 mV, a high exchange current density, and a Tafel slope as small as 55 mV dec⁻¹. The MoC-G also demonstrate similarly good HER activity. Tafel analysis obtained from both the voltammetry data and EIS data reveal the fast reaction kinetics of the MoC-G and Mo₂C-G. Our XPS and XAFS experiments and analyses provide a consistent understanding of the electronic properties of ultrasmall multiple phases molybdenum carbide nanocrystals and their synergetic coupling

Cite this: DOI: 10.1039/c0xx00000x

www.rsc.org/xxxxxx

ARTICLE TYPE

to graphene as origins of the significantly enhanced HER performance.

Acknowledgements

This work was supported by the 100 Talents Project of Chinese Academy of Sciences, China (H9291440S3) and Natural Science Foundation of Guangdong Province, China (DG15313035).

The authors thank beamline BL14W1 of Shanghai Synchrotron Radiation Facility (SSRF) for providing the beam time.

Notes and references

^a Institute of High Energy Physics, Chinese Academy of Sciences (CAS), Beijing 100049, China

^b Dongguan Neutron Science Center, Dongguan 523803, China

* e-mail: taoj@ihep.ac.cn (J. Tao);
hechunyong@ihep.ac.cn (C. He).

Corresponding Author

* e-mail: taoj@ihep.ac.cn (J. Tao); hechunyong@ihep.ac.cn (C. He).

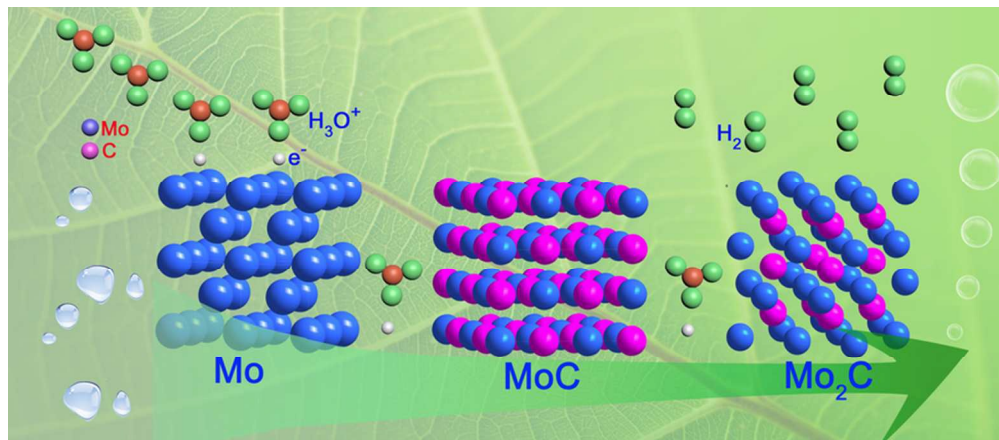
1. T. R. Cook, D. K. Dogutan, S. Y. Reece, Y. Surendranath, T. S. Teets and D. G. Nocera, *Chem. Rev.*, 2010, **110**, 6474-6502.
2. M. Z. Jacobson, W. G. Colella and D. M. Golden, *Science*, 2005, **308**, 1901-1905.
3. J. A. Turner, *Science*, 2004, **305**, 972-974.
4. D. Voiry, H. Yamaguchi, J. Li, R. Silva, D. C. B. Alves, T. Fujita, M. Chen, T. Asefa, V. B. Shenoy, G. Eda and M. Chhowalla, *Nat. Mater.*, 2013, **12**, 850-855.
5. J. Greeley, T. F. Jaramillo, J. Bonde, I. Chorkendorff and J. K. Nørskov, *Nat. Mater.*, 2006, **5**, 909-913.
6. Q. Zeng, J. Bai, J. Li, Y. Li, X. Li and B. Zhou, *Nano Energy*, 2014, **9**, 152-160.
7. G.-R. Xu, J.-J. Hui, T. Huang, Y. Chen and J.-M. Lee, *J. Power Sources*, 2015, **285**, 393-399.
8. R. Subbaraman, D. Tripkovic, D. Strmcnik, K. C. Chang, M. Uchimura, A. P. Paulikas, V. Stamenkovic and N. M. Markovic, *Science*, 2011, **334**, 1256-1260.
9. A. Le Goff, V. Artero, B. Josselme, P. D. Tran, N. Guillet, R. Metaye, A. Fihri, S. Palacin and M. Fontecave, *Science*, 2009, **326**, 1384-1387.
10. J. Zhuo, T. Wang, G. Zhang, L. Liu, L. Gan and M. Li, *Angew. Chem. Int. Ed.*, 2013, **52**, 10867-10870.
11. C. G. Morales-Guio, L.-A. Stern and X. Hu, *Chem. Soc. Rev.*, 2014, **43**, 6555-6569.
12. J. Guo, F. Li, Y. Sun, X. Zhang and L. Tang, *J. Power Sources*, 2015, **291**, 195-200.
13. H. I. Karunadasa, E. Montalvo, Y. Sun, M. Majda, J. R. Long and C. J. Chang, *Science*, 2012, **335**, 698-702.
14. Y. Hou, B. Zhang, Z. Wen, S. Cui, X. Guo, Z. He and J. Chen, *J. Mater. Chem. A*, 2014, **2**, 13795-13800.
15. D.-Y. Wang, M. Gong, H.-L. Chou, C.-J. Pan, H.-A. Chen, Y. Wu, M.-C. Lin, M. Guan, J. Yang, C.-W. Chen, Y.-L. Wang, B.-J. Hwang, C.-C. Chen and H. Dai, *J. Am. Chem. Soc.*, 2015, **137**, 1587-1592.
16. A. R. J. Kucernak and V. N. Naranammalpuram Sundaram, *J. Mater. Chem. A*, 2014, **2**, 17435-17445.
17. Y. Pan, N. Yang, Y. Chen, Y. Lin, Y. Li, Y. Liu and C. Liu, *J. Power Sources*, 2015, **297**, 45-52.
18. Q. Liu, J. Tian, W. Cui, P. Jiang, N. Cheng, A. M. Asiri and X. Sun, *Angew. Chem. Int. Ed.*, 2014, **53**, 6710-6714.
19. Z. Huang, Z. Chen, Z. Chen, C. Lv, M. G. Humphrey and C. Zhang, *Nano Energy*, 2014, **9**, 373-382.
20. S. Han, Y. Feng, F. Zhang, C. Yang, Z. Yao, W. Zhao, F. Qiu, L. Yang, Y. Yao, X. Zhuang and X. Feng, *Adv. Funct. Mater.*, 2015, **25**, 3899-3906.
21. R. Liu, S. Gu, H. Du, A. M. Asiri and C. Li, *J. Mater. Chem. A*, 2014, **2**, 17263-17267.
22. B. Cao, G. M. Veith, J. C. Neufeind, R. R. Adzic and P. G. Khalifah, *J. Am. Chem. Soc.*, 2013, **135**, 19186-19192.
23. W.-F. Chen, K. Sasaki, C. Ma, A. I. Frenkel, N. Marinkovic, J. T. Muckerman, Y. Zhu and R. R. Adzic, *Angew. Chem. Int. Ed.*, 2012, **51**, 6131-6135.
24. Y. Zheng, Y. Jiao, Y. Zhu, L. H. Li, Y. Han, Y. Chen, A. Du, M. Jaroniec and S. Z. Qiao, *Nat. Commun.*, 2014, **5**, 3783.
25. M. Shalom, S. Gimenez, F. Schipper, I. Herraiz-Cardona, J. Bisquert and M. Antonietti, *Angew. Chem. Int. Ed.*, 2014, **53**, 3654-3658.
26. R. B. Levy and M. Boudart, *Science*, 1973, **181**, 547-549.
27. G. Cui, P. K. Shen, H. Meng, J. Zhao and G. Wu, *J. Power Sources*, 2011, **196**, 6125-6130.
28. C. He and P. K. Shen, *Nano Energy*, 2014, **8**, 52-61.
29. A. C. Lausche, J. A. Schaidle and L. T. Thompson, *Appl. Catal., A: Gen.*, 2011, **401**, 29-36.
30. C. Shi, A. Zhang, X. Li, S. Zhang, A. Zhu, Y. Ma and C. Au, *Appl. Catal., A: Gen.*, 2012, **431-432**, 164-170.
31. J. A. Schaidle, A. C. Lausche and L. T. Thompson, *Journal of Catalysis*, 2010, **272**, 235-245.
32. J. Han, J. Duan, P. Chen, H. Lou, X. Zheng and H. Hong, *ChemSusChem*, 2012, **5**, 727-733.
33. G. He, Z. Yan, X. Ma, H. Meng, P. K. Shen and C. Wang, *Nanoscale*, 2011, **3**, 3578-3582.
34. Z. Yan, G. He, P. K. Shen, Z. Luo, J. Xie and M. Chen, *J. Mater. Chem. A*, 2014, **2**, 4014-4022.

Cite this: DOI: 10.1039/c0xx00000x

www.rsc.org/xxxxxx

ARTICLE TYPE

35. H. Vrubel and X. Hu, *Angew. Chem. Int. Ed.*, 2012, **51**, 12703-12706.
36. W. F. Chen, C. H. Wang, K. Sasaki, N. Marinkovic, W. Xu, J. T. Muckerman, Y. Zhu and R. R. Adzic, *Energy Environ. Sci.*, 2013, **6**, 943-951.
37. Q. Lu, G. S. Hutchings, W. Yu, Y. Zhou, R. V. Forest, R. Tao, J. Rosen, B. T. Yonemoto, Z. Cao, H. Zheng, J. Q. Xiao, F. Jiao and J. G. Chen, *Nat. Commun.*, 2015, **6**, 6567.
38. D. H. Youn, S. Han, J. Y. Kim, J. Y. Kim, H. Park, S. H. Choi and J. S. Lee, *ACS Nano*, 2014, **8**, 5164-5173.
39. L. Liao, S. Wang, J. Xiao, X. Bian, Y. Zhang, M. D. Scanlon, X. Hu, Y. Tang, B. Liu and H. H. Girault, *Energy Environ. Sci.*, 2014, **7**, 387-392.
40. H. B. Wu, B. Y. Xia, L. Yu, X.-Y. Yu and X. W. Lou, *Nat. Commun.*, 2015, **6**, 6512.
41. P. Xiao, Y. Yan, X. Ge, Z. Liu, J.-Y. Wang and X. Wang, *Appl. Catal., B: Environ.*, 2014, **154-155**, 232-237.
42. W.-F. Chen, S. Iyer, S. Iyer, K. Sasaki, C.-H. Wang, Y. Zhu, J. T. Muckerman and E. Fujita, *Energy Environ. Sci.*, 2013, **6**, 1818-1826.
43. Z. Yan, G. He, P. K. Shen, Z. Luo, J. Xie and M. Chen, *J. Mater. Chem. A*, 2014, **2**, 4014-4022.
44. C. He and J. Tao, *Chem. Commun.*, 2015, **51**, 8323-8325.
45. O.-H. Kim, Y.-H. Cho, S. H. Kang, H.-Y. Park, M. Kim, J. W. Lim, D. Y. Chung, M. J. Lee, H. Choe and Y.-E. Sung, *Nat. Commun.*, 2013, **4**, 2466.
46. H. Dong, T. Lei, Y. He, N. Xu, B. Huang and C. T. Liu, *Int. J. Hydrogen Energy*, 2011, **36**, 12112-12120.
47. M. Jafarian, O. Azizi, F. Gobal and M. G. Mahjani, *Int. J. Hydrogen Energy*, 2007, **32**, 1686-1693.
48. L. Liao, S. Wang, J. Xiao, X. Bian, Y. Zhang, M. D. Scanlon, X. Hu, Y. Tang, B. Liu and H. H. Girault, *Energy Environ. Sci.*, 2014, **7**, 387-392.
49. B. Łosiewicz, A. Budniok, E. Rówiński, E. Łągiewka and A. Lasia, *Int. J. Hydrogen Energy*, 2004, **29**, 145-157.
50. Y. Li, H. Wang, L. Xie, Y. Liang, G. Hong and H. Dai, *J. Am. Chem. Soc.*, 2011, **133**, 7296-7299.
51. C. Wan, Y. N. Regmi and B. M. Leonard, *Angew. Chem. Int. Ed.*, 2014, **53**, 6407-6410.
52. H. Vrubel, T. Moehl, M. Grätzel and X. Hu, *Chem. Commun.*, 2013, **49**, 8985-8987.
53. L. F. Pan, Y. H. Li, S. Yang, P. F. Liu, M. Q. Yu and H. G. Yang, *Chem. Commun.*, 2014, **50**, 13135-13137.
54. G. E. Haslam, K. Sato, T. Mizokawa, X.-Y. Chin and G. T. Burstein, *Appl. Phys. Lett.*, 2012, **100**, 231601.
55. P. Liu, J. A. Rodriguez and J. T. Muckerman, *J. Phys. Chem. B*, 2004, **108**, 15662-15670.
56. Y. Liang, Y. Li, H. Wang, J. Zhou, J. Wang, T. Regier and H. Dai, *Nat. Mater.*, 2011, **10**, 780-786.
57. Y. Liang, H. Wang, J. Zhou, Y. Li, J. Wang, T. Regier and H. Dai, *J. Am. Chem. Soc.*, 2012, **134**, 3517-3523.



77x33mm (300 x 300 DPI)